Geosci. Model Dev. Discuss., 5, 1691–1741, 2012
www.geosci-model-dev-discuss.net/5/1691/2012/
doi:10.5194/gmdd-5-1691-2012

Geoscientific Model Development Discussions

Lidar signal simulation for the evaluation of aerosols in chemistry-transport models

S. Stromatas[1], S. Turquety[2], L. Menut[1], H. Chepfer[2], J. C. Péré[3], G. Cesana[2], and B. Bessagnet[4]

[1]Institut P.-S. Laplace, Laboratoire de Météorologie Dynamique, CNRS, UMR8539, Ecole Polytechnique, Palaiseau, France
[2]Institut P.-S. Laplace, Laboratoire de Météorologie Dynamique, Université Pierre et Marie Curie-Paris 06, 75252 Paris Cedex 05, France
[3]Laboratoire d'Aérologie, Université Paul Sabatier, CNRS, 14 Avenue Edouard Belin, Toulouse, France
[4]INERIS, Institut National de l'Environnement Industriel et des Risques, Parc technologique ALATA, 60550 Verneuil en Halatte, France

Received: 10 May 2012 – Accepted: 30 May 2012 – Published: 25 June 2012

Correspondence to: S. Stromatas (stavros.stromatas@lmd.polytechnique.fr)

Published by Copernicus Publications on behalf of the European Geosciences Union.

Abstract

We present an adaptable tool, the OPTSIM (OPTical properties SIMulation) software, for the simulation of optical properties and lidar attenuated backscattered profiles (β') from aerosol concentrations calculated by chemistry-transport models (CTM). It was developed to support model evaluation using an original approach based on the lidar Level 1 observations (β'), avoiding the use of Level 2 aerosol retrievals which include specific assumptions on aerosol types that may not be in agreement with the CTM. In addition to an evaluation of the aerosol loading and optical properties, active remote sensing allows the analysis of aerosols' vertical structures. An academic case study for two different species (black carbon and dust) is presented and shows the consistency of the simulator. Illustrations are then given through the analysis of dust events in the Mediterranean region during the summer 2007. These are based on simulations by the CHIMERE regional CTM and observations from the CALIOP space-based lidar, and highlight the potential of this approach to evaluate the concentration, size and vertical structure of the aerosol plumes.

1 Introduction

Aerosols are key for air quality monitoring due to their impact on human health (Pope et al., 2002), visibility (Wang et al., 2009) and biogeochemical cycles (Andreae and Merlet, 2001; Shinn et al., 2000). Through their influence on the Earth radiative budget and cloud microphysics, they also impact meteorological conditions and climate (Forster et al., 2007). In addition to a local effect, aerosol plumes may be transported on long distances with significant direct and indirect effects on atmospheric composition at regional (Bessagnet et al., 2008) to hemispheric scales (Stohl et al., 2002).

While their importance is fully recognized, the assessment of their impact remains poorly quantified due to numerous uncertainties on their emissions, properties and evolution during transport. Model intercomparisons, such as those of the AeroCom

GMDD
5, 1691–1741, 2012

project (e.g. Textor et al., 2007), reveal the need to better quantify the large variabilities in terms of size, morphology and chemical composition of aerosols. More specifically, key species like black carbon (e.g. Koch et al., 2009), mineral dust (e.g. Huneeus et al., 2011) or secondary organic aerosols (e.g. Hallquist et al., 2009) remain generally inadequately modeled, leading to an incomplete description of the aerosol budgets in the atmosphere.

The simulation of the long-range transport of aerosol plumes requires an accurate representation of their vertical structure (location, spread, etc.). It affects the aerosol lifetime (e.g. Keating and Zuber, 2007), and and as a result surface concentrations on surface concentrations but also aerosol-clouds interactions (e.g. Waquet et al., 2009, and references therein) or aerosol radiative forcing (e.g. Zarzycki and Bond, 2010; Zhu et al., 2007).

The availability of satellite observations has greatly enhanced our ability to evaluate models. They complement surface and in situ measurements by providing a large scale context. In particular, the A-Train constellation of satellites allows simultaneous measurements from complementary instrumentation. Passive remote sensors (MODIS on board AQUA or POLDER-3 on board PARASOL) allow the analysis of total aerosol loading through aerosol optical thickness (AOT) retrieval (Remer et al., 2005; Tanré et al., 2011) with good spatio-temporal resolution (almost global daily with pixel size of ~10 km).

These satellite observations have been shown to offer useful insight onto the spatial and temporal variability of particulate matter by both biogenic (e.g. Liu et al., 2008) and anthropogenic sources (e.g. Kaufman et al., 2005). Recent studies have shown their ability to constrain emissions using inverse modeling to estimate their sources (e.g. Dubovik et al., 2008), global budgets (Heald et al., 2010), and surface PM concentrations (van Donkelaar et al., 2006). These observations have also been widely used for the analysis of long range transport pathways (Hodzic et al., 2007; Ridley et al., 2012) and regional simulations of aerosols through their optical properties (Péré et al., 2009).

GMDD
5, 1691–1741, 2012

However, passive satellites provide column-integrated aerosol properties. Thus, they offer limited information on the vertical distribution of aerosols within the atmosphere.

Using the complementary active remote sensing observations by the Cloud-Aerosol Lidar with Orthogonal Polarization (CALIOP) lidar in space (on board CALIPSO, also part of the A-Train) we can obtain valuable information on the vertical distribution of aerosols (Winker et al., 2009). They were used is several recent studies for the evaluation of chemistry-transport model (CTM) simulations (e.g. Yu et al., 2010; Ford and Heald, 2012; Ridley et al., 2012).

The classic approach for comparing model simulations and satellite observations is using the level 2 (L2) retrievals, which are issued from the Level 1 (L1) observations. However, a common discussion point regarding the use of the L2 data is the uncertainty involved due to the specific assumptions made in the data processing. More specifically, the accuracy of these products depends to a large extent on the uncertainties of each step (algorithm) in the processing chain. For example, the estimated values may diverge from the correct values if incorrect estimates of the aerosol layer (e.g. dense smoke layer misclassified as clouds, Liu et al., 2009), aerosol type (e.g. dust misclassified as polluted dust, Omar et al., 2010) and thus lidar ratio are used (Young and Vaughan, 2009). We have chosen to avoid the uncertainties involved in CALIOP aerosol detection and retrieval algorithms (Liu et al., 2009; Omar et al., 2010; Young and Vaughan, 2009; Winker et al., 2009) by using directly the total attenuated backscattered profiles from the CALIOP level 1B V3.01 dataset.

In this paper, we present the OPTSIM post-processing tool, allowing the simulation of L1 lidar satellite data directly. This approach has already been applied for comparisons between airborne lidar measurements and CALIOP for the analysis of field campaigns (de Villiers et al., 2010), for comparisons between model and surface lidar observations (Hodzic et al., 2004), CALIOP observations of clouds (Chepfer et al., 2008) and dust aerosols (Vuolo et al., 2009). Model-derived attenuated backscatter profiles were also used (Generoso et al., 2008) to study dust outflow over the Atlantic, however their method is based on estimations of lidar ratio values. The simulator presented here

GMDD
5, 1691–1741, 2012

generalizes this methodology for the simulation of all types of aerosols, and provides a flexible post-processing tool for chemistry-transport models. For comparisons to models, the profiles that would be observed by a lidar in the same atmospheric conditions as those predicted by the model are calculated.

After a general description of the post-processing simulator for optical properties and lidar signal in Sect. 2, we present a test on an academic case study in Sect. 3. The simulator is then applied on a real test case. We have chosen to evaluate the information provided by the CALIOP observations for the analysis of dust events in the Euro-Mediterranean region, regularly affected by long-range transport of Saharan dust (Querol et al., 2009; Lelieveld, 2002). The observations used are described in Sect. 4 and the CHIMERE CTM in Sect. 5. The results and discussion are presented in Sect. 6.

2 Modeling aerosol optical properties

2.1 Aerosol optical scheme

The first step for modeling aerosol optical properties was to develop an aerosol optical scheme dedicated to the evaluation of vertically integrated particle loading (optical depth) as presented in (Péré et al., 2010). This module was specifically designed to calculate aerosol properties directly comparable to AERONET data and satellite inversions (L2 products). It provides maps of aerosol optical depth (AOD) and other optical properties, such as the Single Scattering Albedo (SSA) and the asymmetry factor (g), based on simulated atmospheric chemical concentration fields.

The AOD or τ_{ext}, which represents the attenuation of the incident solar radiation light by atmospheric particles, depends on the wavelength (λ). For a layer thickness Δz, it is calculated as:

$$\tau_{\text{ext}}(\lambda, z) = \int_{\Delta z} \sigma_p^{\text{ext}}(\lambda, z')\mathrm{d}z' \quad (1)$$

GMDD
5, 1691–1741, 2012

This requires the calculation of the extinction coefficient (by particles), $\sigma_p^{\text{ext}}(z,\lambda)$ [m^{-1}] as:

$$\sigma_p^{\text{ext}}(z,\lambda) = \int_{R_{\min}}^{R_{\max}} \pi R^2 Q_{\text{ext}}(\eta,R,\lambda)\cdot N_p(R,z)\text{d}R \quad (2)$$

where Q_{ext} is the extinction efficiency, depending on the refractive index (η), the particles radius (R) and the wavelength (λ), and N_p is the particle concentration in number (m^{-3}). The complex refractive indices and density values are taken from the ADIENT/APPRAISE technical report (http://www.met.reading.ac.uk/adient/).

The effect of relative humidity on the size of water soluble aerosols and therefore on the refractive index is accounted for by using a growth model as described in (Hänel, 1976). A mean particle density is similarly defined. Finally, in this study, we consider an homogeneous internal mixing of the different chemical species – but a core-shell mixing can also be chosen (user's specifications). For the case of a homogeneous ensemble of spheres, the optical properties for the particles considered are computed using a Mie code (de Rooij and van der Stap, 1984) while for the core-shell mixing scenario, the Wiscombe Mie code for coated spheres is used based on the formulas presented in (Toon and Ackerman, 1981). Non-sphericity of particles such as mineral dust is theoretically and experimentally identified as a source of bias in simulated aerosol optical properties (e.g. Dubovik et al., 2002b) and should be considered cautiously when interpreting the results.

Finally, note that this version of the code is developed for a CTM using a sectional representation of the aerosols population. The size distribution is represented by size sections (bins). Each bin corresponds to a specific diameter range while the cut-off diameters are provided for each bin. This can be modified according to the model configuration. The aerosols size distribution is interpolated to a finer distribution to ensure the best integration as possible where the aerosol concentration number is optically active.

GMDD
5, 1691–1741, 2012

2.2 Lidar signal analysis and modeling

Here we present in more detail a new application included in the simulator: the modeling of the L1 lidar signal. A general overview of the lidar signal modeling is displayed in Fig. 1. The first column represents a model column, where aerosol concentrations (c_i) are available in grid cells for several model levels (z_i). This leads to a vertical concentration profile, where each c_i concentration represent the mean value between z_{i-1} and z_i (z_0 representing the ground). Based on this concentration profile, we simulate the lidar signal that would be observed by a lidar in space (third column) or by a ground based lidar (fourth column).

The calculation of the lidar signal from simulated aerosol concentration fields requires additional parameters than those used for the AOD. These parameters, mainly meteorological, are listed in Table 1.

In order to efficiently compare modeled and measured lidar profiles, the simulator is designed to calculate the Attenuated Scattering Ratio, $R'(z)$. By definition, $R'(z)$ is equal to 1 in absence of aerosols/clouds and when the signal is not attenuated. In the presence of aerosol, $R'(z)$ would be greater than one. Following Winker et al. (2009), this ratio is expressed as:

$$R'(z) = \frac{\beta'(z)}{\beta'_{\mathrm{m}}(z)} \tag{3}$$

where

$$\beta'(z,\lambda) = \left[\frac{\sigma_{\mathrm{m}}^{\mathrm{sca}}(z,\lambda)}{S_{\mathrm{m}}(z,\lambda)} + \frac{\sigma_{\mathrm{p}}^{\mathrm{sca}}(z,\lambda)}{S_{\mathrm{p}}(z,\lambda)}\right] \cdot \exp\left(-2\left[\int_z^{\mathrm{TOA}} \sigma_{\mathrm{m}}^{\mathrm{ext}}(z',\lambda)\mathrm{d}z' + \eta \int_z^{\mathrm{TOA}} \sigma_{\mathrm{p}}^{\mathrm{ext}}(z',\lambda)\mathrm{d}z'\right]\right) \tag{4}$$

GMDD
5, 1691–1741, 2012

and

$$\beta'_{\mathrm{m}}(z,\lambda) = \frac{\sigma_{\mathrm{m}}^{\mathrm{sca}}(z,\lambda)}{S_{\mathrm{m}}(z,\lambda)} \cdot \exp\left(-2\int_{z}^{\mathrm{TOA}} \sigma_{\mathrm{m}}^{\mathrm{ext}}(z',\lambda)\mathrm{d}z'\right) \quad (5)$$

$\beta'(z,\lambda)$ and $\beta'_{\mathrm{m}}(z,\lambda)$ are, respectively the total and molecular attenuated backscatter signal. $\sigma_{\mathrm{p}}^{\mathrm{sca/ext}}(z,\lambda)$ and $\sigma_{\mathrm{m}}^{\mathrm{sca/ext}}(z,\lambda)$ are the extinction/scattering coefficients for particles and molecules (in km^{-1}). S_{m} (respectively S_{p}) is the molecular (respectively particular) extinction-to-backscatter ratio (in sr). Note that S_{m} is directly linked to the backscattering phase function P_{π} with

$$S_{\mathrm{m}} = 4\pi/P_{\pi} \quad [\mathrm{sr}^{-1}] \quad (6)$$

Finally, $\eta(z)$ represents the particles multiple scattering and z represents the distance between the emitter and the studied point. Note that for the case of a space lidar the integration begins from the top of the atmosphere (TOA) while for a ground lidar the integration begins from 0 (ground level) to z.

The molecular contribution (σ_{m} and S_{m}) is calculated theoretically as in (Collins and Russell, 1976). For altitudes below 100 km and when the vertical distribution of pressure (P) and temperature (T) is known, the backscattering coefficient can be expressed as:

$$\sigma_{\mathrm{m}}^{\mathrm{sca}} = \frac{P}{k_{\mathrm{B}}T} \cdot s_{\mathrm{sca,mol}}(\pi) \quad (7)$$

with k_{B} being the Boltzmann constant and $s_{\mathrm{sca,mol}}$ the molecular scattering cross section (in $\mathrm{m}^2\,\mathrm{sr}^{-1}$), given by:

$$s_{\mathrm{sca,mol}} = 5.45 \cdot \left(\frac{\lambda}{0.55}\right)^{-4.09} \cdot 10^{-32} \quad (8)$$

GMDD
5, 1691–1741, 2012

The molecular extinction coefficient σ_m^{ext} is given as a function of σ_m^{sca}:

$$\sigma_m^{ext} = \frac{8\pi}{3} \cdot \sigma_m^{sca} \tag{9}$$

The particles contribution (σ_p and S_p) can be written as a function of the particle concentration (N_p in m^{-3}) and on the particle scattering/extinction efficiency ($Q_{sca/ext}$) which depends on the refractive index, the size of particles and the wavelength (λ) (cf. Eq. 2).

Note that multiple scattering effects are not taken into account here (η is set to 1 in Eq. 4). The single scattering approximation is adequate for small optical depths and non-absorbing aerosols (Gordon, 1997). However, large scattering particles such as mineral dust could lead to non-negligible multiple scattering effects (e.g. Wandinger et al., 2010).

Finally, we also simulate the color ratio (χ') which corresponds to the ratio between two lidar profiles observed simultaneously at two different wavelengths ($\lambda_1 = 1064$ nm and $\lambda_2 = 532$ nm) :

$$\chi'(z) = \frac{R'_{\lambda_1}(z)}{R'_{\lambda_2}(z)} == \frac{\beta'_{\lambda_1}(z)}{\beta'_{\lambda_2}(z)} \tag{10}$$

Since scattering is more efficient when the wavelength is of the same order of magnitude as the particle diameter, this ratio provides information of the size of the particles in the backscattering layers and hence on their nature (cloud droplets, dust or pollution aerosols for instance). χ' is expected to be lower than 1 for small particles compared to wavelengths. It allows the qualitative identification of large/small particles but since there is a significant overlap between the distributions of χ' for different aerosol types, it cannot be used directly as an aerosol type identification tool (Omar et al., 2010).

For flexibility and computational efficiency, the optical code and the lidar simulator are intentionally designed to process a series of profiles. As our purpose is to compare

GMDD
5, 1691–1741, 2012

the model simulations with satellite retrievals (or ground measurements) a preparatory code is used to co-locate spatially (±0.25°) and temporally (±30 min) and extract the necessary parameters (henceforth as profiles) from the outputs of the model according to the satellite orbit track (or surface site location) selected.

3 Simulator validation with an academic test case

In order to validate each step of the calculation, an academic case study is conducted considering simplified atmospheric conditions: only one species and a constant concentration in selected size sections and altitude levels.

The species selected for this demonstration are black carbon (BCAR) and mineral dust (DUST). The main difference between these species is that BCAR is strongly absorbing while the amount of extinction of the solar radiation from DUST is resulting from scattering.

3.1 Configuration of the simulator

For this case study, we distribute a 5 ppbv concentration (~17–20 $\mu g\,m^{-3}$ depending on altitude) in only one of the size sections of the model at a time. The size distribution for this academic test case is characterized by 8 initial bins (from 40 nm to 10 µm, cf. Table 2) and is extended to 40 bins inside the code (log-normal interpolation). We also consider 18 vertical levels extending from the surface to 200 hPa. Vertically, the concentration is located in the lower troposphere, between ~700 and ~1200 m. This configuration allows us to identify the variability of the calculated parameters as a function of the particle's size.

The refractive indices used for the calculation of their optical properties are shown in Table 3.

The scattering and extinction efficiencies calculated for this configuration are shown on Fig. 2. The evolution of these efficiencies as a function of particle size and

GMDD
5, 1691–1741, 2012

wavelength will determine the behavior of the particles' optical properties (and thus of the AOD) as well as the lidar signal, as discussed below.

First of all, in order to verify the correct computation of the AOD in our code, we calculate independently the theoretical AOD that would result from such conditions and compare them with our results. We achieve an agreement of 99.63 % for the total theoretical AOD. On average, the simulator presents a small negative bias (truncation error). The main source of this bias originates from the interpolation to 40 size sections which affects the computation of Q_{ext} and Q_{sca}. The choice of 40 bins (instead of the initial 8) is made as a function of desired accuracy and computation time (not shown here). For the theoretical case, we also have calculated the total optical depth using finer discretization of the size sections. The overall bias of this choice was found to converge to +7 % for the total AOD (for 40×10^5 bins).

3.1.1 Aerosol optical depth

The AOD computed at 532 nm for the configuration described above and for each vertical level (18 in total) is presented in Fig. 3. As expected, we observe an increase at altitude levels where the concentration was located.

For the BCAR case, the highest value ($\tau = 0.053$) is reached when the aerosol load is distributed in the 0.156–0.312 µm bin. AOD is also higher for an increase in the smallest size range (<0.078 µm bin) than in the largest one (5–10 µm), with maximum AOD of $\tau = 0.030$ and $\tau = 0.001$, respectively. This is explained by the evolution of the number concentration (N) of the particles, which decreases from 1.86×10^{11} m^{-3} in the 1st bin to 0.6×10^5 m^{-3} in the 8th bin, while the mass concentration remains constant. As a result, the maximum AOD is shifted to smaller sizes than that of maximum extinction efficiency (0.312–0.625 µm bin for 532 nm), where N is larger.

A similar behavior is observed for the DUST case. The AOD (for $\lambda = 532$ nm) presents its maximum (0.019) in the 0.312–0.625 µm bin as a function of the scattering/extinction efficiency and of the number concentration of particles.

GMDD
5, 1691–1741, 2012

3.1.2 Attenuated backscatter coefficient

The β' profiles calculated for this academic case (for both species) at two different wavelengths ($\lambda = 532$ et 1064 nm) are plotted in Fig. 4, showing a behavior similar to that of the AOD. Its dependence on the aerosol size and, as a result, on $Q_{ext/sca}$ and N, is highlighted in the BCAR case for example, by a maximum value ($3.35 \times 10^{-6}\,W\,m^2\,sr^{-1}$) in the 0.156–0.312 µm bin in the ~ 700–1200 m altitude layer. Similarly, its maximum ($1.39 \times 10^{-6}\,W\,m^2\,sr^{-1}$) at 1064 nm is obtained for the 0.312–0.625 µm bin.

Below the simulated plume (<828 m), β' (at 532 nm) decreases due to the extinction by the aerosol layer during integration from the TOA to the surface. At 1064 nm where the extinction is small, β' values return to the same values as before the aerosol layer. This is less pronounced but still observed in the DUST case where the extinction is of smaller magnitude (Fig. 3).

3.1.3 Scattering and color ratios

The $R'(z)$ and $\chi'(z)$ profiles associated to the β' presented above (Fig. 4) is shown in the Fig. 5a. Its variations are directly related to those of β' for both species.

For really small particles ($R/\lambda < 0.1$) the $\beta'_{1064}/\beta'_{532}$ ratio is almost constant. In this case, extinction controls the evolution of χ' with altitude (Fig. 5b). At the 0.312–0.625 µm bin where extinction at 1064 nm is maximum and the backscattering coefficient β becomes higher (Fig. 2) than the one at 532 nm, we obtain $\beta'_{1064} > \beta'_{532}$. Consequently, χ' reaches its highest value. When the two β coefficients begin to converge, extinction is decreasing which results in a decrease of χ'.

GMDD
5, 1691–1741, 2012

4 Observations

Our simulator allows the calculation of a series of optical properties that can be directly compared to observations. In this section, the main observations that can be analyzed using this simulator are briefly described.

4.1 Aerosol optical thickness

4.1.1 Surface sunphotometers

The AERONET sun photometers network (Holben et al., 1998) provides ground solar extinction measurements at several wavelengths (e.g. 440, 675, 870 and 1020 nm) are used to derive the aerosol optical depth and Angström's exponent. In addition, sky radiance measurements in the almucantar and principle plane geometries used to derive several other aerosol optical properties (e.g. volume size distribution, refractive index and single scattering albedo) through an inversion algorithm (Dubovik and King, 2000). The combination of those products provides valuable information on various aerosol characteristics (e.g. size, shape, composition). These measurements are also very useful for validating aerosol products obtained from satellite sensors and evaluating the performance of CTMs, in simulating the optical properties of aerosols.

Among the AERONET retrieval products available, we use the level 2.0 cloud screened and quality-assured retrievals such as the aerosol optical depth at 500 nm (with a fine and coarse mode separation) and Angström's exponent in order to evaluate our simulation and identify the bias of the model into simulating aerosols. The accuracy and the uncertainty in AERONET measurements are described in (Dubovik and et al., 2000).

The reader is referred to (Péré et al., 2010) for an example of comparisons between model simulations and AERONET observations using the optical module.

GMDD
5, 1691–1741, 2012

4.1.2 Passive satellite remote sensing with MODIS

The Moderate-Resolution Imaging Spectroradiometer (MODIS) on board TERRA since 1999 and AQUA since 2002, performs measurements used to identify the spatial and temporal characteristics of the aerosol load both over land and ocean (Remer et al., 2005) based on two different algorithms. Its orbit is sun-synchronous at an altitude of 705 km. It has a viewing swath width of 2330 km and views the entire surface of the Earth every one to two days. For the aerosol retrievals, it makes use of seven (0.47–2.13 µm) of the total 36 channels (0.41–15 µm). Its spatial resolution is 250 m to 1 km in the nadir (250 m × 250 m at 644 nm and 855 nm, 500 m × 500 m at the other 5 spectral bands). Aerosol products are provided at a spatial resolution of 10 km × 10 km (20 × 20 pixels of 500 m × 500 m resolution).

In this study, we use the MODIS/Aqua collection 5.1 level 2 data. The retrieved AOD (τ) is estimated to be accurate to ±0.05 (±0.15·τ) over the land and ±0.03 (±0.05·τ) over the ocean (Levy et al., 2010). MODIS is also known to correlate well with the AERONET sunphotometer measurements. (Bréon et al., 2011) report a correlation of 0.829/0.904 with a RMSD of 0.118/0.125 for the total AOD at 500 nm over ocean/land and a slight positive bias (+0.02).

4.2 Lidar vertical profiles with CALIOP

The simulator can be used for the comparison to surface or space-based lidar observations. Since the application examples are focused on satellite observations from the CALIPSO mission, it is here briefly introduced.

4.2.1 CALIOP data characteristics

The CALIOP lidar is operating since April 2006 on board the sun-synchronous satellite CALIPSO as a part of the A-train constellation. It measures vertical backscatter profiles from aerosols and clouds at 532 nm and 1064 nm in the troposphere and lower

GMDD
5, 1691–1741, 2012

stratosphere (Winker et al., 2009) with a nadir-viewing geometry (14-days revisit time). The L1 processing consists of three-dimensional geo-location followed by calibration (Powell and al., 2009).

The resulting Level 1B data (with a horizontal resolution of 333 m) contain molecular density profiles (MD), profiles of total attenuated backscatter coefficient (β') at the two wavelengths, and profiles of cross polarized attenuated backscatter (β'_{perp}) at 532 nm. The vertical resolution of the 532 nm channel is altitude-dependent from 30 m (up to 8.2 km) to 1000 m × 60 m (8.2–20.2 km), while it is 1000 m × 60 m up to 20.2 km for the 1064 nm channel, with a total of 583 vertical levels distributed from the surface up to 40 km. The Molecular Density profile (MD) is derived from Goddard Modeling and Assimilation Office (GMAO) atmospheric profiles (Bey et al., 2001) for 33 vertical levels between the surface and 40 km.

Uncertainty sources on L1B data include possible calibration biases, lidar scattering signal noise (shot noise) and background noise (e.g. Winker et al., 2009; Powell and al., 2009). As the daytime measurements contain higher noise levels than night time measurements due to solar background signals (e.g. Hunt et al., 2009), we will limit our analyses to night-time observations only.

4.2.2 Computation of the observed attenuated scattering ratio (R'_{obs})

For the purposes of our comparisons we compute the scattering ratio (R') following the same method as in (Chepfer et al., 2010). The basic methodology described in their Sect. 2.1 is reminded in the following.

First, the measured attenuated backscattered profile (β' over 583 vertical levels) and the MD profile (33 vertical levels) are each independently averaged or interpolated onto 80-level vertical levels (240 m thick), leading to the β'_{vert} and MD_{vert} profiles. This averaging significantly increases the β' signal-to-noise ratio. The initial horizontal resolution (333 m) is kept in order to screen the small boundary layer clouds (next section).

To convert the MD profile into molecular profile β'_{mol}, the β'_{vert} and MD_{vert} profiles are analyzed and averaged in cloud-free portions of the stratosphere ($22 < z < 25$ km

GMDD
5, 1691–1741, 2012

for night time data). At these altitudes, β'_{vert} and MD_{vert} profiles are each averaged horizontally over ±33 profiles (±10 km) on both sides of a given profile.

The ratio between these two values ($< \beta'_{vert} > / < MD_{vert} >$ is then used to scale the MD_{vert} profile into an attenuated backscatter molecular signal profile ($\beta'_{vert,mol}$). The latter is the β'_{mol} profile that would be measured in the absence of clouds and aerosols in the atmosphere. The measured lidar attenuated scattering ratio profile (R'_{obs}) is then computed by dividing the β'_{vert} profile by the $\beta'_{vert,mol}$ profile. Its horizontal resolution is 330 m and the vertical resolution is 240 m.

Pixels located below and at the surface level are rejected by using the "altitude-elevation" flag from level 1 CALIOP data.

4.2.3 Cloud screening in the observations

Clouds dominate the received signal and as a result the contribution of aerosols is undermined in cloudy situations. Since we are primarily interested in aerosols, a cloud filter will be used to eliminate cloud-contaminated profiles. Boundary layer clouds can have a small horizontal extension, even lower than 1 km (e.g. Medeiros et al., 2010; Koren et al., 2008; Konsta et al., 2012). For this reason we need to use high horizontal resolution R' profiles for cloud detection.

The threshold on R' used to detect clouds (or aerosols) is altitude and resolution dependent, due to the nature of the noise imposed on the lidar backscatter signal. It presents lower values in regions of (relatively) high clear air SNR, and higher threshold values in low clear air SNR (e.g. high altitude) regions. Here the lidar profile is considered to be cloud-contaminated when $R' \geq 7.5$ is detected in a 3-profiles running average (1 km, used to reduce noise level). This threshold value ($R' = 7.5$) has been adjusted based on sensitivity studies (not shown) using lidar profiles at the resolution used here (240 m vertical and 330 m horizontal, as in Chepfer et al., 2010).

For optically thick clouds (typically with optical depth larger than 3), the lidar signal is fully attenuated below the cloud, and the pixels located below cloud are filtered out.

GMDD
5, 1691–1741, 2012

For high altitude clouds with moderate optical depth (<3, typically cirrus clouds), the lidar signal is attenuated in the observations (R' can be lower than 1) below the cloud, but above the top model level depending on the model's configuration. This attenuation will then not be accounted for in the model, and an artificial bias may occur between modeled and observed R'. To avoid this problem, the observed R' is forced to 1 at the top model boundary. The required scaling factor is applied to the whole profile. Otherwise, only the peak at the cloud location is removed.

Finally, the cloud-free data are averaged at the model's horizontal and vertical resolutions for direct comparison to the simulated R' profiles.

4.2.4 Aerosol detection limits

The nighttime aerosol detection threshold used here is $R = 1.2$ for the 532 nm channel (Chepfer et al., 2012). Using this threshold value (which is considered to be an upper limit since we are averaging profiles), a theoretical calculation of the minimum detectable concentration per species (one at a time) and size section was conducted. The corresponding results are shown in Fig. 6. We notice that a crucial parameter in determining these values, is the size and number concentration of the particles, as explained in Sect. 3.1.1.

The minimum detectable concentration for each species using a typical size distribution for urban, suburban and rural areas, is also calculated. In general, for concentrations in the lower troposphere (cf. Sect. 3.1) the median for the minimum detectable concentration for all species considered is between ~ 2.4 and $\sim 5.5\,\mu g\,m^{-3}$ (BC 4.7, OC 3.8, H_2SO_4 5.5, HNO_3 2.4, NH_3 3.4, SALT 3.3 and SOA $3.2\,\mu g\,m^{-3}$). The highest concentration value is observed for mineral dust (median $11.3\,\mu g\,m^{-3}$). Comparing with orders of magnitudes observed in different locations in Europe (Putaud et al., 2010), these limits of detection will be generally exceeded in polluted conditions (urban), but they are below or close to the limits in rural and suburban sites.

GMDD
5, 1691–1741, 2012

5 Meteorology and chemistry-transport modeling

In this study, the WRF meteorological and CHIMERE chemistry-transport models are used. Since CHIMERE is an off-line model, we have to provide the necessary meteorological fields from WRF. We use the same model configuration as in studies such as (Rouil et al., 2009) and (Bessagnet et al., 2010). For this study, the modeling system WRF+CHIMERE simulated the period from 29 June to 6 September 2007 while both meteorology and chemical concentrations results are obtained with an hourly frequency.

5.1 The CHIMERE regional CTM

The CHIMERE multi-scale model is designed to provide concentration fields for 44 gas-phase and aerosol species, given an initial set of NO_x, SO_x, NH_3, PM, VOCs (Volatile Organic Compounds) and CO emissions. In this study, the latest version of CHIMERE (chimere2011b) is used, covering the Euro-Mediterranean domain from 4° W to 34° E in longitude and from 24.7° N to 45.4° N in latitude, with a horizontal resolution of 20 km. The vertical grid contains 18 uneven layers starting from the surface pressure level and reaching 200 hPa.

A detailed model documentation is available online (http://www.lmd.polytechnique.fr/chimere/). A description of the model's dynamics and gas-phase parts is given in (Schmidt et al., 2001) while some improvements (Vautard et al., 2005; Bessagnet et al., 2009) have been made since. The thermodynamic equilibrium model ISORROPIA (Nenes et al., 1998), implemented on-line in CHIMERE, is used to determine the particle/gas partitioning of semi-volatile inorganic species. The surface emissions account for anthropogenic, biogenic, mineral dust and fires sources. The anthropogenic emissions preprocessing is described in Menut et al. (2012). The MEGAN model (Guenther et al., 2006) is used for the biogenic emissions while the mineral dust emissions are described in Menut (2008).

GMDD
5, 1691–1741, 2012

Regarding particulate matter, extensive intercomparisons at a regional scale can be found in (Vautard et al., 2007). Furthermore, the model's ability to correctly reproduce mineral dust emissions and transport in Europe was shown in (Bessagnet et al., 2008). In the study of (Vuolo et al., 2009) it is shown that the model is able to simulate the climatology of Western African aerosols with a tendency to overestimate the vertical diffusion of the plumes.

The aerosols species considered by the model are sulfates, nitrates, ammonium, organic aerosols and sea-salt (Bessagnet et al., 2010). For a detailed description of the aerosol module in CHIMERE, the reader is referred to (Bessagnet et al., 2004). The particle size distribution ranges from about 40 nm to 10 µm, distributed into 8 bins between the following size intervals: 0.039, 0.078, 0.156, 0.312, 0.625, 1.25, 2.5, 5, 10 µm.

5.2 The WRF meteorological model

The mesoscale model Weather Research and Forecasting (WRF) is used in its 3.2.1 version and in its non-hydrostatic configuration. Two nested domains are defined in order to model the synoptic scale over a large African-Euro-Mediterranean domain and the local scale with an included Mediterranean domain. In this study, the results are presented only for the smallest domain, the coarse domain is used to produce more.

A lambert projection is chosen for the horizontal grid with a a regular spacing of $\Delta x = \Delta y = 20$ km. The vertical grid covers 32 levels from the surface to 50 hPa with an integration time step of 4 min. For the microphysics, the WRF Single Moment-5 class scheme is used (Hong et al., 2004). The radiation scheme used is RRTMG with the MCICA method of random cloud overlap (Mlawer et al., 1997). The surface layer scheme is based on Monin-Obukhov with Carslon-Boland viscous sub-layer. Surface physics are calculated using the Noah Land Surface Model scheme with four soil temperature and moisture layers (Chen and Dudhia, 2001). The planetary boundary layer

GMDD
5, 1691–1741, 2012

physics are processed using the Yonsei University scheme (Hong et al., 2006) and the cumulus parameterization uses the ensemble scheme of (Grell and Devenyi, 2002).

6 Analysis of dust events in the Euro-Mediterranean area during the summer 2007

Mineral dust is well known to contribute to atmospheric pollution in urban areas in addition to local anthropogenic pollutants over the Euro-Mediterranean region (e.g. Bessagnet et al., 2008; Querol et al., 2009). Transported mainly from the Sahara desert (Laurent et al., 2008), it often results in an exceedance of the air quality thresholds in the most concerned countries like Spain (e.g. Escudero et al., 2007), Italy (e.g. Gobbi et al., 2007) or Greece (e.g. Kaskaoutis et al., 2008).

6.1 Comparisons to AERONET and MODIS AOD

The general situation during the summer 2007 was first analyzed using comparisons between the CHIMERE simulation and retrievals from the AERONET network for the total AOD at 500 nm. Figure 7 shows the results at several observation sites around the Mediterranean Basin. The agreement is good for background levels and most events are captured in the Carpentras and Lecce sites (correlations of 63 % and 56 %, respectively). The highest AOD values are observed at the Blida site (North of Algeria), which is particularly well suited for the analysis of dust impact in the Euro-Mediterranean region since it is located within the Northern Saharan domain. The correlation between model and observations is 58 %, the bias (model-observation) is −0.25 with a RSME 0.28 for the AOD (500 nm). The Angström exponent at 440–870 nm and the contribution of dust to the total aerosol load in the model simulation is shown in Fig. 8. Several major dust events were detected, with large AOD and low Angström exponent values (desert dust aerosols are caracterised by low α values, ranging generally from ~ 1.2 down to ~ -0.1 (e.g. Dubovik et al., 2002a). The very good agreement of the model for

GMDD
5, 1691–1741, 2012

the low values suggests that the size distributions are correctly simulated for the dust events. But the peak AOD values in the observations are generally underestimated in the model.

We have chosen to analyze more specifically two events, for which CALIOP measurements are also available (see following section): 7–9 July 2007 (well captured in the simulation) and 13–15 July 2007 (underestimated). The model shows large increase in dust load for the two events, corresponding to transport from emissions in the Algerian part of the Sahara desert. However, it is significantly lower for the 13–15 July 2007 event than for the 7–9 July 2007 event. The transport pathways for the 2nd event show that the bulk of the dust plume is located to the East for the Blida site. The strong underestimate may thus be due to both underestimate of the emissions and transport error.

For those two events, the corresponding AOD distributions observed by MODIS and calculated based on the CHIMERE simulations are shown in Fig. 9. According to the observations, both events were characterized by intense dust emissions, covering the west-northern part of Africa and resulting in AOD (at 550 nm) values up to 0.93 while a large plume was observed moving northeastward over the Mediterranean Basin. The comparisons for the 7–9 July 2007 time period show that the simulated transport of the plume is consistent with the observations but also that its intensity and extent are underestimated. For the second event, a small, very local, dust plume is simulated but its intensity and extent are missed.

6.2 Comparisons to CALIOP observations

For each of the events presented in the previous section, the corresponding CALIPSO orbit is plotted in Fig. 10 along with the corresponding AOD (for λ = 532 nm) simulated by OPTSIM.

For the 7–9 July event, the CALIOP observations show an aerosol layer around 35° N near the Blida station, extending vertically from ~3 to ~5.5 km (~2.5 km large), and above the sea in the northeastward direction at ~1 to 3 km altitude. For this event, the

GMDD
5, 1691–1741, 2012

general structure of the plume is well reproduced in the CHIMERE simulation. However, its vertical extent is overestimated. Three individual R' profiles are presented in Fig. 14: one corresponding to the maximum observed R' (35.19° N); the second located over the sea (39.23° N); the third (33.91° N) closer to the area of the dust emissions. According to CHIMERE, the dominant species in both cases is dust (97.3 % and 93.5 %) although in the second profile (over the sea) we see a higher contribution of sea salt above the surface level (3.5 %). For the entire portion of the orbit within the simulated domain, the mean altitude of the maximum simulated R' is 4.51 km against 2.93 km for CALIPSO, with a RSME of 2.53 km and a correlation 0.45.

The model R' value is underestimated near the observed peak and overestimated over the Mediterranean sea. This may be related to a slight temporal shift in the emissions and/or transport. The average maximum simulated R' presents a correlation of 0.6 with the observed R', a mean bias of 1.12 and a RSME of 0.68.

For the 14 July 2007, the simulated R' show enhancements around 3–4 km high above the southern portion of the orbit, which is consistent with the large plume observed at 4 km. Here again, the model strongly underestimates R' and overestimates the plume's vertical extent.

For the two time periods, the color ratios (Fig. 12) are underestimated in the model. Examining the first event, the corresponding simulated effective radius (R_{eff}) also shown in Fig. 12 presents a maximum (~1.2–1.3 µm) near the observed CR peak but at a higher altitude. As seen in Fig. 14, it corresponds mostly to dust particles. However, R_{eff} provides information on the mean size of particles while CR strongly depends on the size distribution (cf. Fig. 5). For instance, higher R_{eff} values may be associated with lower CR values (e.g. ~35° N compared to ~39° N values, corresponding to profiles in Fig. 14) when the concentration in smaller size sections is higher. More specifically, around ~35° N at the same altitude as the R_{eff} peak, the simulated size distribution is dominated by the 8th size section. By inverting the concentration between the 8th and the 7th, so that the total concentration remains unaltered, we notice an increase of 63.6 % in CR along with a 8.4 % decrease in R_{eff}. This suggests that although the mean

GMDD
5, 1691–1741, 2012

size of the particles and their localization may well represented in the model (consistent with the Angström exponent comparisons), a revision of the dust size distribution would be beneficial for the CR comparisons.

The main discrepancy in the simulated transport is the plume's vertical extent. This overestimation in CHIMERE may be due to the chosen vertical resolution, which decreases to ~1 km in the free troposphere. The comparisons suggest a need for a higher vertical resolution, in order to achieve a better accuracy in terms of layer thickness, which could be beneficial to the model's ability to reproduce transport and vertical mixing of atmospheric constituents.

But the vertical diffusion parameterization in the model may also cause too large transport towards higher altitudes. The R' underestimation for the profile closest to the emissions area may be attributed to an underestimation of the dust emissions as we have also seen in the AOD comparisons.

7 Conclusions

In this paper we presented the OPTSIM post-processing tool, designed for a complete comparison of aerosol concentration distributions calculated by chemistry-transport models (CTM) to passive and active remote-sensing observations. By simulating the aerosol optical properties and column integrated parameters (e.g. AOD, Angström exp.) it allows an evaluation of the horizontal and temporal distributions of aerosol compared to passive remote-sensing observations. Furthermore, by simulating lidar attenuated backscattered profiles, the aerosol vertical structures in the model simulations can be directly compared to calibrated Level 1B CALIOP observations. Therefore, it allows additionally, an evaluation of the vertical structure of aerosols and as a result, the evaluation of the vertical mixing and transport parametrizations in the model. Finally, by simulating color ratio profiles, it can identify problems related to the mean size and the modeled size distribution of aerosols ratio while the contribution of each species to the

GMDD
5, 1691–1741, 2012

simulated lidar signal can also be quantified and therefore can be used for the study of specific pollution events.

The methodology used and the requirements of the OPTSIM tool in terms of model output configuration are first described. The validation of the simulator's self-consistency is then demonstrated on an academic case study. For two different species (black carbon and dust), the main steps of the calculation from simulated concentration profiles are detailed: optical depth, attenuated backscattered profile, and finally attenuated scattering ratio and color ratio profiles.

An application of this tool is presented for the evaluation of the simulation by the CHIMERE CTM of two specific dust events that took place in the Northwestern African region during July 2007. Firstly, an analysis of these events is conducted based on comparisons to the AERONET and MODIS passive observations only. Then a comparison of the simulated lidar profiles with CALIOP L1 observations is undertaken. Since we are focusing only on aerosol plumes, the data have to be cloud-filtered before they are averaged on the same horizontal and vertical grid as the model for comparison. The general structure of the dust plume is well simulated while the intensity of the examined events appears underestimated. The model appears positively biased regarding the thickness and the altitude of the plume, especially near the emissions area. An assumption of a slight temporal shift in the emissions and/or transport can also be made from the underestimated R' values near the observed peak and overestimated values over the Mediterranean sea. These discrepancies may be partly attributed to the vertical mixing parametrization which may have to be revised with the addition of finer altitude layers.

This work shows the additional information that can be expected from the use of lidar observation for the analysis of long-range transport events. However, due to their limited horizontal coverage, the complementary use of passive remote-sensing observations is necessary for further validation of the emissions and horizontal transport pathways.

GMDD
5, 1691–1741, 2012

The OPTSIM tool described in this paper was designed to be model independent and can be adapted for other CTMs. It can be provided upon request to any interested user.

Acknowledgements. The authors are grateful to the French ICARE database (http://www.icare.univ-lille1.fr/) for providing the MODIS and CALIPSO data. The MODIS and CALIPSO project and science teams are greatly acknowledged for data availability as well as CLIMSERV/CGTD for providing access to the Level 1 CALIPSO dataset. The authors acknowledge the Centre National des Etudes Spatiales (CNES, France) for financial support. S. Stromatas is supported by a fellowship from the CNES and the Agence de l'Environnement et de la Maitrise de l'Energie (ADEME, France).

The publication of this article is financed by CNRS-INSU.

References

Andreae, M. O. and Merlet, P.: Emission of trace gases and aerosols from biomass burning, Global Biogeochem. Cy., 15, 995–966, 2001. 1692

Bessagnet, B., Hodzic, A., Vautard, R., Beekmann, M., Cheinet, S., Honore, C., Liousse, C., and Rouil, L.: Aerosol modeling with CHIMERE – preliminary evaluation at the continental scale, Atmos. Environ., 38, 2803–2817, 2004. 1709

Bessagnet, B., Menut, L., Aymoz, G., Chepfer, H., and Vautard, R.: Modeling dust emissions and transport within Europe: the Ukraine March 2007 event, J. Geophys. Res., 113, D15202, doi:10.1029/2007JD009541, 2008. 1692, 1709, 1710

GMDD

5, 1691–1741, 2012

Bessagnet, B., Menut, L., Curci, G., Hodzic, A., Guillaume, B., Liousse, C., Moukhtar, S., Pun, B., Seigneur, C., and Schulz, M.: Regional modeling of carbonaceous aerosols over Europe – focus on secondary organic aerosols, J. Atmos. Chem., 61, 175–202, 2009. 1708

Bessagnet, B., Seigneur, C., and Menut, L.: Impact of dry deposition of semi-volatile organic compounds on secondary organic aerosols, Atmos. Environ., 44, 1781–1787, doi:10.1016/j.atmosenv.2010.01.027, 2010. 1708, 1709

Bey, I., Jacob, D. J., Yantosca, R. M., Logan, J. A., Field, B. D., Fiore, A. M., Li, Q., Liu, H. Y., Mickley,L. J., and Schultz, M. G.: Global modeling of tropospheric chemistry with assimilated meteorology: Model description and evaluation J. Geophys. Res., 106, 23073–23096, doi:10.1029/2001JD000807, 2001.

Bréon, F., Vermeulen, A., and Descloitres, J.: An evaluation of satellite aerosol products against sunphotometer measurements, Remote Sens. Environ., 115, 3102–3111, 2011. 1704

Chen, F. and Dudhia, J.: Coupling an advanced land surface-hydrology model with the Penn State-NCAR MM5 modeling system. Part I: model implementation and sensitivity, Mon. Weather Rev., 129, 569–585, 2001. 1709

Chepfer, H., Bony, S., Winker, D., Chiriaco, M., Dufresne, J., and Sèze, G.: Use of CALIPSO lidar observations to evaluate the cloudiness simulated by a climate model, Geophys. Res. Lett., 35, L15704, doi:10.1029/2008GL034207, 2008. 1694

Chepfer, H., Bony, S., Winker, D., Cesana, G., Dufresne, J. L., Minnis, P., Stubenrauch, C. J., and Zeng, S.: The GCM Oriented CALIPSO Cloud Product (CALIPSO-GOCCP), J. Geophys. Res., 115, D00H16, doi:10.1029/2009JD012251, 2010. 1705, 1706

Chepfer, H., Cesana, G., Winker, D., Getzewich, B., and Vaughan, M.: Comparison of two different cloud climatologies derived from CALIOP Level 1 observations: the CALIPSO-ST and the CALIPSO-GOCCP, J. Atmos. Ocean. Tech., in press, 2012. 1707

Collins, R. T. H. and Russell, P. B.: Lidar measurement of particles and gases by elastic backscattering and differential absorption, Top. Appl. Phys., 14, 71–151, 1976. 1698

de Rooij, W. A. and van der Stap, C. C. A. H.: Expansion of Mie scattering matrices in generalized spherical functions, Astron. Astrophys., 131, 237–248, 1984. 1696

de Villiers, R. A., Ancellet, G., Pelon, J., Quennehen, B., Schwarzenboeck, A., Gayet, J. F., and Law, K. S.: Airborne measurements of aerosol optical properties related to early spring transport of mid-latitude sources into the Arctic, Atmos. Chem. Phys., 10, 5011–5030, doi:10.5194/acp-10-5011-2010, 2010. 1694

GMDD

5, 1691–1741, 2012

Dubovik, O. and King, M.: A flexible inversion algorithm for retrieval of aerosol optical properties from sun and sky radiance measurements, J. Geophys. Res., 105, 20673–20696, 2000. 1703

Dubovik, O., Smirnov, A., Holben, B. N., King, M. D., Kaufman, Y. J., Eck, T. F., and Slutsker, I.: Accuracy assessments of aerosol optical properties retrieved from Aerosol Robotic Network (AERONET) sun and sky radiance measurements, J. Geophys. Res., 105, 9791–9806, 2000. 1703

Dubovik, O., Holben, B. N., Eck, T., Smirnov, A., Kaufman, Y. J., King, M. D., Tanré, D., and Slutsker, I.: Variability of absorption and optical properties of key aerosol types observed in worldwide locations, J. Atmos. Sci., 59, 590–608, 2002a. 1710

Dubovik, O., Holben, B. N., Lapyonok, T., Sinyuk, A., Mishchenko, M. I., Yang, P., and Slutsker, I.: Non-spherical aerosol retrieval method employing light scattering by spheroids, Geosphys. Res. Lett, 29, 1415, 2002b. 1696

Dubovik, O., Lapyonok, T., Kaufman, Y. J., Chin, M., Ginoux, P., Kahn, R. A., and Sinyuk, A.: Retrieving global aerosol sources from satellites using inverse modeling, Atmos. Chem. Phys., 8, 209–250, doi:10.5194/acp-8-209-2008, 2008. 1693

Escudero, M., Querol, X., Avila, A., and Cuevas, E.: Origin of the exceedances of the European daily PM limit value in regional background areas of Spain, Atmos. Environ., 41, 730–744, 2007. 1710

Ford, B. and Heald, C. L.: An A-Train and model perspective on the vertical distribution of aerosols and CO in the Northern Hemisphere, J. Geophys. Res., 117, D06211, doi:10.1029/2011JD016977, 2012. 1694

Forster, P., Ramaswamy, V., Artaxo, P., Berntsen, T., Betts, R., Fahey, D., Haywood, J., Lean, J., Lowe, D., Myhre, G., Nganga, J., Prinn, R., Raga, G., Schulz, M., and Dorland, R. V.: Changes in atmospheric constituents and in radiative forcing, in: Climate Change 2007: The Physical Science Basis. Contribution of Working Group I to the Fourth Assessment Report of the Intergovernmental Panel on Climate Change, edited by: Solomon, S., Qin, D., Manning, M., Chen, Z., Marquis, M., Averyt, K. B., Tignor, M., and Miller, H. L., Cambridge University Press, Cambridge, UK and New York, NY, USA, 2007. 1692

Generoso, S., Bey, I., Labonne, M., and Bréon, F. M.: Aerosol vertical distribution in dust outflow over the Atlantic: comparisons between GEOS-Chem and Cloud-Aerosol Lidar and Infrared Pathfinder Satellite Observation (CALIPSO), J. Geophys. Res., 113, D24209, doi:10.1029/2008JD010154, 2008. 1694

GMDD

5, 1691–1741, 2012

Gobbi, G., Barnaba, F., and Ammannat, L.: Estimating the impact of Saharan dust on the year 2001 PM_{10} record of Rome, Italy, Atmos. Environ., 41, 261–275, 2007. 1710
Gordon, H.: Atmospheric correction of ocean color imagery in the Earth Observing System era, J. Geophys. Res., 102, 17081–17106, 1997. 1699
Grell, G. A. and Devenyi, D.: A generalized approach to parameterizing convection combining ensemble and data assimilation techniques, Geophys. Res. Lett., 29, 1693, doi:10.1029/2002GL015311, 2002. 1710
Guenther, A., Karl, T., Harley, P., Wiedinmyer, C., Palmer, P. I., and Geron, C.: Estimates of global terrestrial isoprene emissions using MEGAN (Model of Emissions of Gases and Aerosols from Nature), Atmos. Chem. Phys., 6, 3181–3210, doi:10.5194/acp-6-3181-2006, 2006. 1708
Hallquist, M., Wenger, J. C., Baltensperger, U., Rudich, Y., Simpson, D., Claeys, M., Dommen, J., Donahue, N. M., George, C., Goldstein, A. H., Hamilton, J. F., Herrmann, H., Hoffmann, T., Iinuma, Y., Jang, M., Jenkin, M. E., Jimenez, J. L., Kiendler-Scharr, A., Maenhaut, W., McFiggans, G., Mentel, Th. F., Monod, A., Prévôt, A. S. H., Seinfeld, J. H., Surratt, J. D., Szmigielski, R., and Wildt, J.: The formation, properties and impact of secondary organic aerosol: current and emerging issues, Atmos. Chem. Phys., 9, 5155–5236, doi:10.5194/acp-9-5155-2009, 2009. 1693
Hänel, G.: The properties of atmospheric particles as functions of the relative humidity at thermodynamic equilibrium with surrounding moist air, Adv. Geophys., 19, 73–188, 1976. 1696
Heald, C., Ridley, D., Kreidenweis, S., and Drury, E. E.: Satellite observations cap the atmospheric organic aerosol budget, Geophys. Res. Lett., 37, L24808, doi:10.1029/2010GL045095, 2010. 1693
Hodzic, A., Chepfer, H., Vautard, R., Chazette, P., Beekmann, M., Bessagnet, B., Chatenet, B., Cuesta, J., Drobinski, P., Goloub, P., Haeffelin, M., and Morille, Y.: Comparison of aerosol chemistry transport model simulations with lidar and sun photometer observations at a site near Paris, J. Geophys. Res., 109, D23201, doi:10.1029/2004JD004735, 2004. 1694
Hodzic, A., Madronich, S., Bohn, B., Massie, S., Menut, L., and Wiedinmyer, C.: Wildfire particulate matter in Europe during summer 2003: meso-scale modeling of smoke emissions, transport and radiative effects, Atmos. Chem. Phys., 7, 4043–4064, doi:10.5194/acp-7-4043-2007, 2007. 1693
Holben, B., Eck, T., Slutsker, I., Tanré, D., Buis, J., Setzer, A., Vermote, E., Reagan, J., Kaufman, Y., Nakajima, T., Lavenu, F., Jankowiak, I., and Smirnov, A.: AERONET: a federated

GMDD
5, 1691–1741, 2012

instrument network and data archive for aerosol characterization, Remote Sens. Environ., 66, 1–16, 1998. 1703

Hong, S. Y., Dudhia, J., and Chen, S.: A revised approach to ice microphysical processes for the bulk parameterization of clouds and precipitation, Mon. Weather Rev., 132, 103–120, 2004. 1709

Hong, S. Y., Noh, Y., and Dudhia, J.: A new vertical diffusion package with an explicit treatment of entrainment processes, Mon. Weather Rev., 134, 2318–2341, doi:10.1175/MWR3199.1, 2006. 1710

Huneeus, N., Schulz, M., Balkanski, Y., Griesfeller, J., Prospero, J., Kinne, S., Bauer, S., Boucher, O., Chin, M., Dentener, F., Diehl, T., Easter, R., Fillmore, D., Ghan, S., Ginoux, P., Grini, A., Horowitz, L., Koch, D., Krol, M. C., Landing, W., Liu, X., Mahowald, N., Miller, R., Morcrette, J.-J., Myhre, G., Penner, J., Perlwitz, J., Stier, P., Takemura, T., and Zender, C. S.: Global dust model intercomparison in AeroCom phase I, Atmos. Chem. Phys., 11, 7781–7816, doi:10.5194/acp-11-7781-2011, 2011. 1693

Hunt, W. H., Winker, D. M., Vaughan, M. A., Powell, K. A., Lucker, P. L., and Weimer, C.: CALIPSO lidar description and performance assessment, J. Atmos. Ocean. Tech., 7, 1214–1228, 2009. 1705

Kaskaoutis, D., Kambezidis, H., Nastos, P., and Kosmopoulos, P.: Study on an intense dust storm over Greece, Atmos. Environ., 42, 6884–6896, 2008. 1710

Kaufman, Y. J., Boucher, O., Tanré, D., Chin, M., Remer, L. A., and Takemura, T.: Aerosol anthropogenic component estimated from satellite data, Geophys. Res. Lett., 32, L17804, doi:10.1029/2005GL023125, 2005. 1693

Keating, T. J. and Zuber, A.: Hemispheric Transport of Air Pollution 2007 Interim Report, United Nations, Economic Commission for Europe, Geneva, 2007. 1693

Koch, D., Schulz, M., Kinne, S., McNaughton, C., Spackman, J. R., Balkanski, Y., Bauer, S., Berntsen, T., Bond, T. C., Boucher, O., Chin, M., Clarke, A., De Luca, N., Dentener, F., Diehl, T., Dubovik, O., Easter, R., Fahey, D. W., Feichter, J., Fillmore, D., Freitag, S., Ghan, S., Ginoux, P., Gong, S., Horowitz, L., Iversen, T., Kirkevåg, A., Klimont, Z., Kondo, Y., Krol, M., Liu, X., Miller, R., Montanaro, V., Moteki, N., Myhre, G., Penner, J. E., Perlwitz, J., Pitari, G., Reddy, S., Sahu, L., Sakamoto, H., Schuster, G., Schwarz, J. P., Seland, Ø., Stier, P., Takegawa, N., Takemura, T., Textor, C., van Aardenne, J. A., and Zhao, Y.: Evaluation of black carbon estimations in global aerosol models, Atmos. Chem. Phys., 9, 9001–9026, doi:10.5194/acp-9-9001-2009, 2009. 1693

GMDD

5, 1691–1741, 2012

Lidar signal simulation for the evaluation of aerosols

S. Stromatas et al.

Konsta, D., Chepfer, H., and Dufresne, J.: A process oriented description of tropical oceanic clouds for climate model evaluation, based on a statistical analysis of daytime A-train high spatial resolution observations, Clim. Dynam., in press, 2012. 1706

Koren, I., Oreopoulos, L., Feingold, G., Remer, L. A., and Altaratz, O.: How small is a small cloud?, Atmos. Chem. Phys., 8, 3855–3864, doi:10.5194/acp-8-3855-2008, 2008. 1706

Laurent, B., Marticorena, B., Bergametti, G., Léon, J. F., and Mahowald, N. M.: Modeling mineral dust emissions from the Sahara desert using new surface properties and soil database, J. Geophys. Res., 113, D14218, doi:10.1029/2007JD009484, 2008. 1710

Lelieveld, J., Berresheim, H., Borrmann, S., Crutzen, P. J., Dentener, F. J., Fischer, H., Feichter, J., Flatau, P. J., Heland, J., Holzinger, R., Korrmann, R., Lawrence, M. G., Levin, Z., Markowicz, K. M., Mihalopoulos, N., Minikin, A.,Ramanathan, V., de Reus, M., Roelofs, G. J., Scheeren, H. A., Sciare, J., Schlager, H., Schultz, M., Siegmund, P., Steil, B., Stephanou, E. G., Stier, P., Traub, M., Warneke, C., Williams, J., and Ziereis, H.: Global air pollution crossroads over the Mediterranean, Science, 298, 794, doi:10.1126/science.1075457, 2002. 1695

Levy, R. C., Remer, L. A., Kleidman, R. G., Mattoo, S., Ichoku, C., Kahn, R., and Eck, T. F.: Global evaluation of the Collection 5 MODIS dark-target aerosol products over land, Atmos. Chem. Phys., 10, 10399–10420, doi:10.5194/acp-10-10399-2010, 2010. 1704

Liu, Z., Omar, A., Vaughan, M., Hair, J., and Kittaka, C.: CALIPSO lidar observations of the optical properties of Saharan dust: a case study of long-range transport, J. Geophys. Res., 113, D07207, doi:10.1029/2007JD008878, 2008. 1693

Liu, Z., Vaughan, M., Winker, D., Kittaka, C., Getzewich, B., Kuehn, R., Omar, A., Powell, K., Trepte, C., and Hostetler, C.: The CALIPSO lidar cloud and aerosol discrimination: version 2 algorithm and initial assessment of performance, J. Atmos. Ocean. Tech., 26, 1198–1213, 2009. 1694

Medeiros, B., Nuijens, L., Antoniazzi, C., and Stevens, B.: Low-latitude boundary layer clouds as seen by CALIPSO, J. Geophys. Res., 115, D23207, doi:10.1029/2010JD014437, 2010. 1706

Menut, L.: Sensitivity of hourly Saharan dust emissions to NCEP and ECMWF modelled wind speed, J. Geophys. Res.-Atmos., 113, D16201, doi:10.1029/2007JD009522, 2008. 1708

Menut, L., Goussebaile, A., Bessagnet, B., Khvorostiyanov, D., and Ung, A.: Impact of realistic hourly emissions profiles on modelled air pollutants concentrations, Atmos. Environ., 49 , 233–244, 2012. 1708

GMDD

5, 1691–1741, 2012

Mlawer, E., Taubman, S., Brown, P., Iacono, M., and Clough, S.: Radiative transfer for inhomogeneous atmospheres: RRTM a validated correlated-k model for the longwave, J. Geophys. Res., 102, 16663–16682, 1997. 1709

Nenes, A., Pilinis, C., and Pandis, S.: ISORROPIA: a new thermodynamic model for inorganic multicomponent atmospheric aerosols, Aquat. Geochem., 4, 123–152, 1998. 1708

Omar, A., Winker, D. M., Vaughan, M. A., Hu, Y., Trepte, C. R., Ferrare, R. A., Lee, K.-P., Hostetler, C. A., Kittaka, C., Rogers, R. R., Kuehn, R. E., and Liu, Z.: The CALIPSO automated aerosol classification and lidar ratio selection algorithm, J. Atmos. Ocean. Tech., 26, 1994–2014, 2010. 1694, 1699

Péré, J. C., Mallet, M., Bessagnet, B., and Pont, V.: Evidence of the aerosol core-shell mixing state over Europe during the heat wave of summer 2003 by using CHIMERE simulations and AERONET inversions, Geophys. Res. Lett., 36, L09807, doi:10.1029/2009GL037334, 2009. 1693

Péré, J., Mallet, M., Pont, V., and Bessagnet, B.: Evaluation of an aerosol optical scheme in the chemistry-transport model CHIMERE, Atmos. Environ., 44, 3688–3699, doi:10.1016/j.atmosenv.2010.06.034, 2010. 1695, 1703

Pope, C. A., Burnett, R. T., Thun, M. J., Calle, E. E., Krewski, D., and Thurston, K. I. G. D.: Lung cancer, cardiopulmonary mortality, and long-term exposure to fine particulate air pollution, JAMA-J. Am. Med. Assoc., 287, 1132–1141, 2002. 1692

Powell, K. A., Hostetler, C. A., Liu, Z., Vaughan, M. A., Kuehn, R. E., Hunt, W. H., Lee, K.-P., Trepte, C. R., Rogers, R. R., Young, S. A., and Winker, D. M.: CALIPSO lidar calibration algorithms. Part I: nighttime 532 nm parallel channel and 532 nm perpendicular channel, J. Atmos. Ocean. Tech., 26, 2015–2033, 2009. 1705

Putaud, J.-P., Van Dingenen, R., Alastuey, A., Bauer, H., Birmili, W., Cyrys J., Flentje, H., Fuzzi, S., Gehrig, R., Hansson, H. C., Harrison, R. M., Herrmann, H., Hitzenberger, R., Hüglin, C., Jones, A. M., Kasper-Giebl, A., Kiss, G., Kousam, A., Kuhlbusch, T. A. J., Löschau, G., Maenhaut, W., Molnar, A., Moreno, T., Pekkanen, J., Perrino, C., Pitz, M., Puxbaumc, H., Querol, X., Rodriguez, S., Salma, I., Schwarz, J., Smolik, J., Schneider, J., Spindler, G., ten Brink, H., Tursic, J., Viana, M., Wiedensohler, A., and Raes, F.: A European aerosol phenomenology – 3: physical and chemical characteristics of particulate matter from 60 rural, urban, and kerbside sites across Europe, Atmos. Environ., 44, 1308–1320, 2010. 1707

Querol, X., Pey, J., Pandolfi, M., Alastuey, A., Cusack, M., Pereza, N., Moreno, T., Viana, M., Mihalopoulos, N., Kallo, G., and Kleanthous, S.: African dust contributions to mean ambient

GMDD

5, 1691–1741, 2012

PM_{10} mass-levels across the Mediterranean Basin, Atmos. Environ., 43, 4266–4277, 2009. 1695, 1710

Remer, L. A., Kaufman, Y. J., Tanré, D., Mattoo, S., Chu, D. A., Martins, J. V., Li, R.-R., Ichoku, C., Levy, R. C., Kleidman, R. G., Eck, T. F., Vermote, E., and Holben, B. N.: The MODIS aerosol algorithm, products and validation, special section, J. Atmos. Sci., 62, 947–973, 2005. 1693, 1704

Ridley, D. A., Heald, C. L., and Ford, B.: North African dust export and deposition: a satellite and model perspective, J. Geophys. Res., 117, D02202, doi:10.1029/2011JD016794, 2012. 1693, 1694

Rothman, L. S., Gordon, I. E., Barbe, A., Chris Benner, D., Bernath, P. F., Birk, M., Boudon, V., Brown, L. R., Campargue, A., Champion, J.-P., Chance, K., Coudert, L. H., Dana, V., Devi, V. M., Fally, S., Flaud, J.-M., Gamache, R. R., Goldmanm, A., Jacquemart, D., Kleiner, I., Lacome, N., Lafferty, W. J., Min, J.-Y., Massie, S. T., Mikhailenko, S. N., Miller, C. E., Moazzen-Ahmadi, N., Naumenko, O. V., Nikitin, A. V., Orphal, J., Perevalov, V. I., Perrin, A., Predoi-Cross, A., Rinsl, C. P., Rotger, M., Šimečková, M., Smith, M. A. H., Sung, K., Tashkun, S. A., Tennyson, J., Toth, R. A., V aele, A. C., and Ver Auwera, J.: The HITRAN 2008 molecular spectroscopic database, J. Quant. Spectrosc. Ra., 100, 533–572, 2009. 1727

Rouil, L., Honore, C., Vautard, R., Beekmann, M., Bessagnet, B., Malherbe, L., Meleux, F., Dufour, A., Elichegaray, C., Flaud, J., Menut, L., Martin, D., Peuch, A., Peuch, V., and Poisson, N.: PREV'AIR: an operational forecasting and mapping system for air quality in Europe, B. Am. Meteorol. Soc., 90, 73–83, doi:10.1175/2008BAMS2390.1, 2009. 1708

Schmidt, H., Derognat, C., Vautard, R., and Beekmann, M.: A comparison of simulated and observed ozone mixing ratios for the summer of 1998 in Western Europe, Atmos. Environ., 35, 6277–6297, 2001. 1708

Shinn, E., Smith, G., Prospero, J., Betzer, P., Hayes, M., Garrison, V., and Barber, R.: African dust and the demise of caribbean coral reefs, Geophys. Res. Lett., 27, 3029–3032, 2000. 1692

Stohl, A., Eckhardt, S., Forster, C., James, P., and Spichtinger, N.: On the pathways and timescales of intercontinental air pollution transport, J. Geophys. Res., 107, 4684, 2002. 1692

Tanré, D., Bréon, F. M., Deuzé, J. L., Dubovik, O., Ducos, F., François, P., Goloub, P., Herman, M., Lifermann, A., and Waquet, F.: Remote sensing of aerosols by using polarized,

GMDD

5, 1691–1741, 2012

directional and spectral measurements within the A-Train: the PARASOL mission, Atmos. Meas. Tech., 4, 1383–1395, doi:10.5194/amt-4-1383-2011, 2011. 1693

Textor, C., Schulz, M., Guibert, S., Kinne, S., Balkanski, Y., Bauer, S., Berntsen, T., Berglen, T., Boucher, O., Chin, M., Dentener, F., Diehl, T., Feichter, J., Fillmore, D., Ginoux, P., Gong, S., Grini, A., Hendricks, J., Horowitz, L., Huang, P., Isaksen, I. S. A., Iversen, T., Kloster, S., Koch, D., Kirkevåg, A., Kristjansson, J. E., Krol, M., Lauer, A., Lamarque, J. F., Liu, X., Montanaro, V., Myhre, G., Penner, J. E., Pitari, G., Reddy, M. S., Seland, Ø., Stier, P., Takemura, T., and Tie, X.: The effect of harmonized emissions on aerosol properties in global models – an AeroCom experiment, Atmos. Chem. Phys., 7, 4489–4501, doi:10.5194/acp-7-4489-2007, 2007. 1693

Toon, O. and Ackerman, T.: Algorithms for the calculation of scattering by stratified spheres, Appl. Optics, 20, 3657–3660, 1981. 1696

van Donkelaar, A., Martin, R. V., and Park, R. J.: Estimating ground-level $PM_{2.5}$ using aerosol optical depth determined from satellite remote sensing, J. Geophys. Res., 111, D21201, doi:10.1029/2005JD006996, 2006. 1693

Vautard, R., Bessagnet, B., Chin, M., and Menut, L.: On the contribution of natural Aeolian sources to particulate matter concentrations in Europe: testing hypotheses with a modelling approach, Atmos. Environ., 39, 3291–3303, 2005. 1708

Vautard, R., Maidi, M., Menut, L., Beekmann, M., and Colette, A.: Boundary layer photochemistry simulated with a two-stream convection scheme, Atmos. Environ., 41, 8275–8287, 2007. 1709

Vuolo, M., Chepfer, H., Menut, L., and Cesana, G.: Comparison of mineral dust layers vertical structures modelled with CHIMERE-DUST and observed with the CALIOP lidar, J. Geophys Res.-Atmos, 114, D09214, doi:10.1029/2008JD011219, 2009. 1694, 1709

Wandinger, U., Tesche, M., Seifert, P., Ansmann, A., Müller, D., and Althausen, D.: Size matters: influence of multiple scattering on CALIPSO lightextinction profiling in desert dust, Geophys. Res. Lett., 37, L10801, doi:10.1029/2010GL042815, 2010. 1699

Wang, K., Dickinson, R. E., and Liang, S.: Clear sky visibility has decreased clear sky visibility has decreased over land globally from 1973 to 2007, Science, 323, 1468–1470, 2009. 1692

Waquet, F., Riédi, J., Labonnote, L.-C., Goloub, P., Cairns, B., Deuzé, J.-L., and Tanré, D.: Aerosol remote sensing over clouds using A-Train observations, J. Atmos. Sci., 66, 2468–2480, 2009. 1693

GMDD

5, 1691–1741, 2012

Winker, D. M., Vaughan, A. O., Hu, Y., Powell, K. A., Liu, Z., Hunt, W. H., and Young, S. A.: Overview of the CALIPSO mission and CALIOP data processing algorithms, J. Atmos. Ocean. Tech., 26, 2310–2323, 2009. 1694, 1697, 1705

Young, S. and Vaughan, M.: The retrieval of profiles of particulate extinction from cloud-aerosol lidar infrared pathfinder satellite observations (CALIPSO) data: algorithm description, J. Atmos. Ocean. Tech., 26, 1105–1119, 2009. 1694

Yu, H., Chin, M., Winker, D. M., Omar, A. H., Liu, Z., Kittaka, C., and Diehl, T.: Global view of aerosol vertical distributions from CALIPSO lidar measurements and GOCART simulations: regional and seasonal variations, J. Geophys. Res., 115, D00H30, doi:10.1029/2009JD013364, 2010. 1694

Zarzycki, C. M. and Bond, T. C.: How much can the vertical distribution of black carbon affect its global direct radiative forcing?, Geophys. Res. Lett., 37, L20807, doi:10.1029/2010GL044555, 2010. 1693

Zhu, A., Ramanathan, V., Li, F., and Kim, D.: Dust plumes over the Pacific, Indian, and Atlantic oceans: climatology and radiative impact, J. Geophys. Res., 112, D16208, doi:10.1029/2007JD008427, 2007. 1693

GMDD

5, 1691–1741, 2012

Table 1. List of variables required as input to the OPTSIM software, and their corresponding name to be read in a netCDF input file for the default version of the code. N_z corresponds to the number of vertical layers in the profiles, N_b to the number of size bins, and N_{obs} to the number of observations to be processed.

Variable	Data and dimensions		Units
Time	Time	(N_{obs})	h
Longitude	lon	(N_{obs})	degrees
Latitude	lat	(N_{obs})	degrees
Meteorology			
Temperature	temp	$(N_{obs} \times N_z)$	K
Air density	airmloc	$(N_{obs} \times N_z)$	molecules cm^{-3}
Relative humidity	rh	$(N_{obs} \times N_z)$	%/100
Altitude	hlay	$(N_{obs} \times N_z)$	m
Atmospheric composition			
Concentration	conc	$(N_{obs} \times N_z \times N_b)$	µg m^{-3}
Cut-off diameters	cut_off_diameters	(N_b)	m

GMDD
5, 1691–1741, 2012

Table 2. Theoretical and calculated AOD at λ = 532 nm per size section.

Bin	Size	Aerosol Optical Depth		
	Diameter (μm)	Theoretical	Simulated	Error (%)
1	0.039–0.078	0.3434	0.3467	0.9720
2	0.078–0.156	0.4682	0.4788	2.2726
3	0.156–0.312	0.5939	0.5858	−1.3714
4	0.312–0.625	0.3574	0.3485	−2.4892
5	0.625–1.250	0.1617	0.1587	−1.8692
6	1.250–2.500	0.0743	0.0732	−1.4374
7	2.500–5.000	0.0348	0.0345	−0.8607
8	5.000–10.00	0.0166	0.0165	−0.5518
Total		2.0502	2.0427	
Mean				−0.6669

GMDD
5, 1691–1741, 2012

Table 3. List of species accounted for by the CHIMERE optical module, wavelength-dependent complex refractive index and density of each aerosol species. All refractive indices and density values are taken from the ADIENT/APPRAISE technical report (http://www.met.reading.ac.uk/adient/).

Species	Model Species	Refractive index 532 nm	Refractive index 1064 nm
Organic carbon	OCAR	$1.63–2.32 \times 10^{-2} i$	$1.63–7.0 \times 10^{-4} i$
Black carbon	BCAR	$1.85–7.10 \times 10^{-1} i$	$1.85–7.10 \times 10^{-1} i$
Mineral dust	DUST	$1.53–1.20 \times 10^{-3} i$	$1.53–7.74 \times 10^{-4} i$
Secondary organic aerosols	SOA	$1.56–3.0 \times 10^{-3} i$	$1.56–3.0 \times 10^{-3} i$
Equivalent sulfate	H2SO4	$1.44–1.0 \times 10^{-8} i$	$1.42–1.64 \times 10^{-6} i$
Equivalent nitrate	HNO3	$1.61–0 i$	$1.59–1.8 \times 10^{-5} i$
Equivalent ammonium	NH3	$1.53–1.0 \times 10^{-7} i$	$1.51–2.35 \times 10^{-6} i$
Sea salt	SALT	$1.50–1.20 \times 10^{-8} i$	$1.47–1.97 \times 10^{-4} i$
Water*	H2O	$1.333–1.9 \times 10^{-9} i$	$1.326–4.18 \times 10^{-6} i$

* HITRAN database, (Rothman et al., 2009).

GMDD
5, 1691–1741, 2012

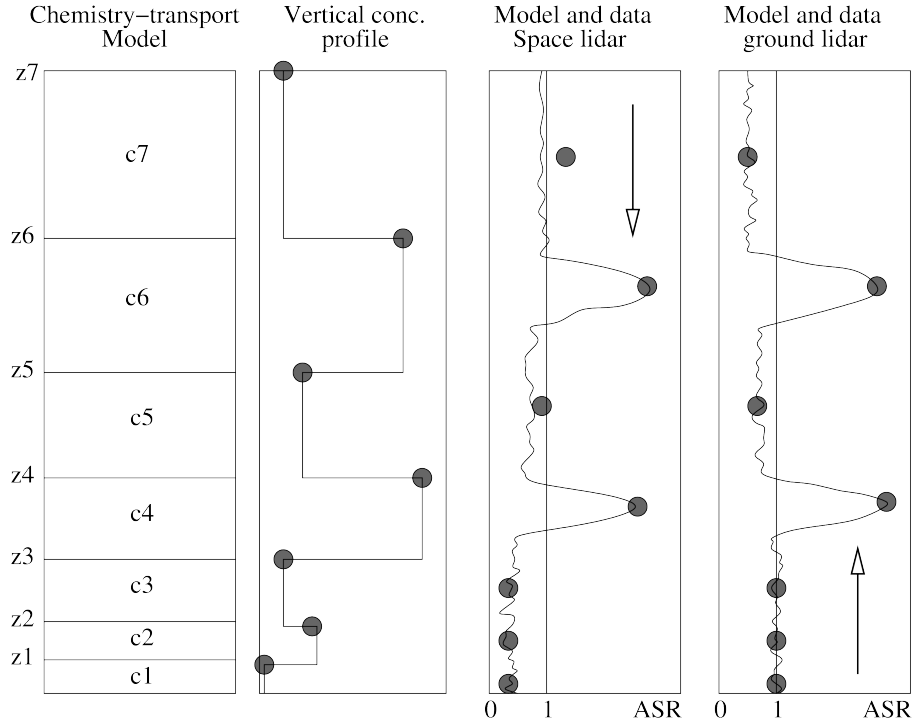

Fig. 1. Overview of the comparison methodology: example of the modeled $R'(z)$ estimation from initial concentration profiles (middle-left panel) on a specific model vertical grid (left panel) in the case of a space lidar (middle-right panel) or a ground lidar (right panel). The grey dots correspond to the value reported in the model simulation.

GMDD
5, 1691–1741, 2012

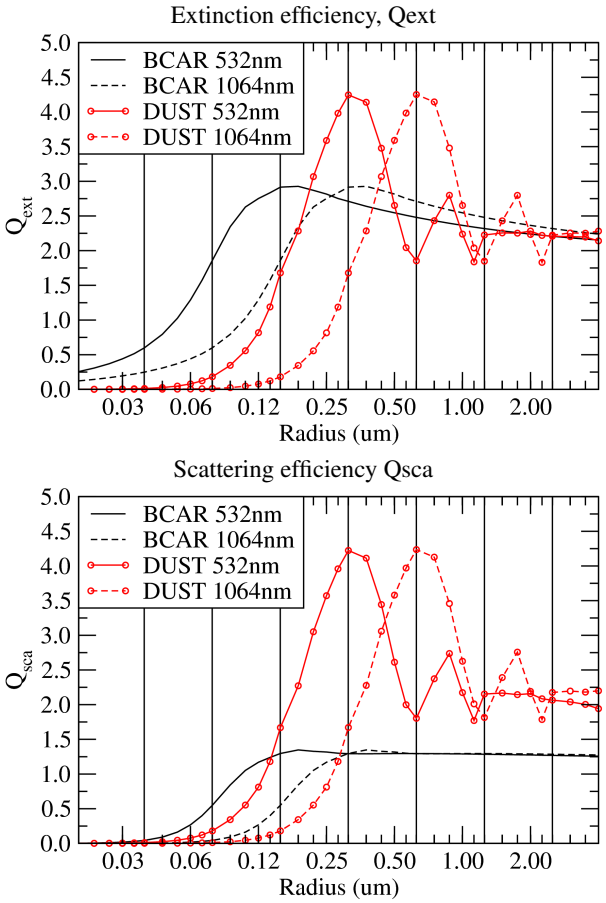

Fig. 2. Black carbon (BCAR) and mineral dust (DUST) extinction (Q_{ext}) and scattering (Q_{sca}) efficiencies as a function of size (radius) for 2 different wavelengths (λ = 532, 1064 nm).

GMDD
5, 1691–1741, 2012

Lidar signal simulation for the evaluation of aerosols

S. Stromatas et al.

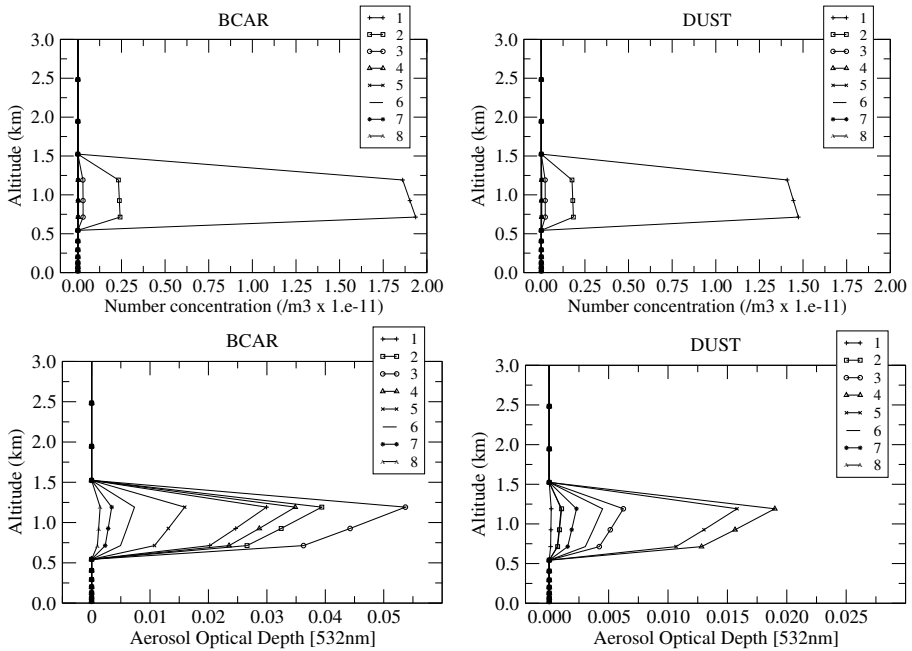

Fig. 3. Profiles of BCAR and DUST concentrations in number and AOD per size section (bin) as a function of altitude, and for a wavelength of 532 nm.

GMDD
5, 1691–1741, 2012

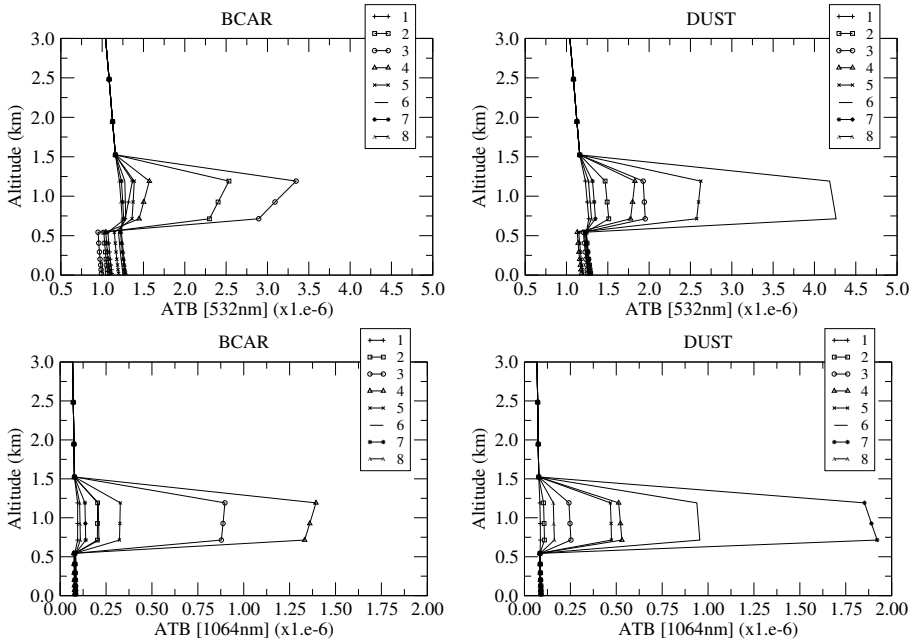

Fig. 4. Profiles of β' for BCAR (left) and DUST (right), per size section (bin) as a function of altitude for λ = 532, 1064 nm.

GMDD
5, 1691–1741, 2012

Lidar signal simulation for the evaluation of aerosols

S. Stromatas et al.

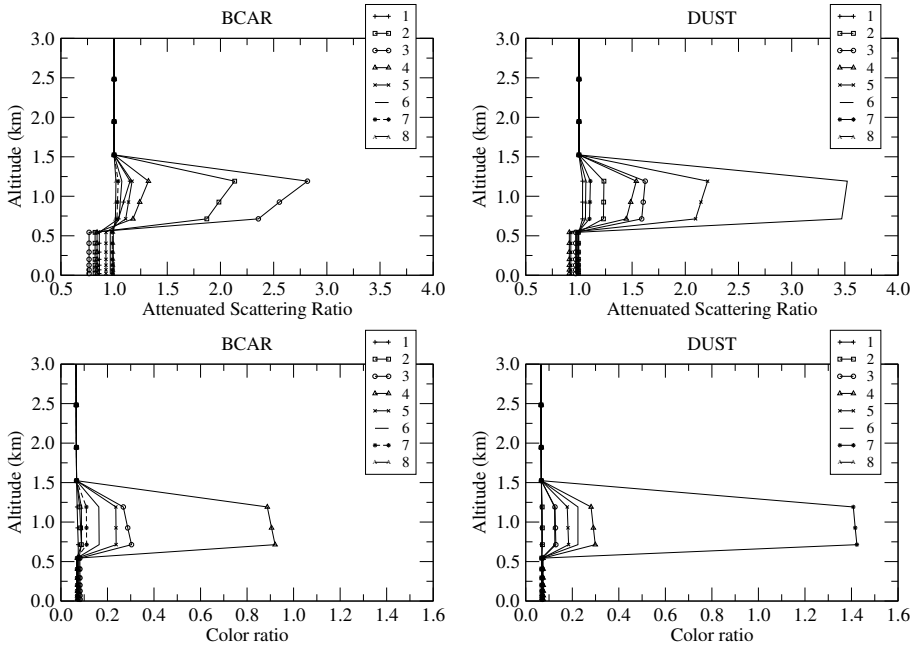

Fig. 5. Profiles of attenuated scattering ratio and color ratio for BCAR (left) and DUST (right) per size section as a function of altitude.

GMDD
5, 1691–1741, 2012

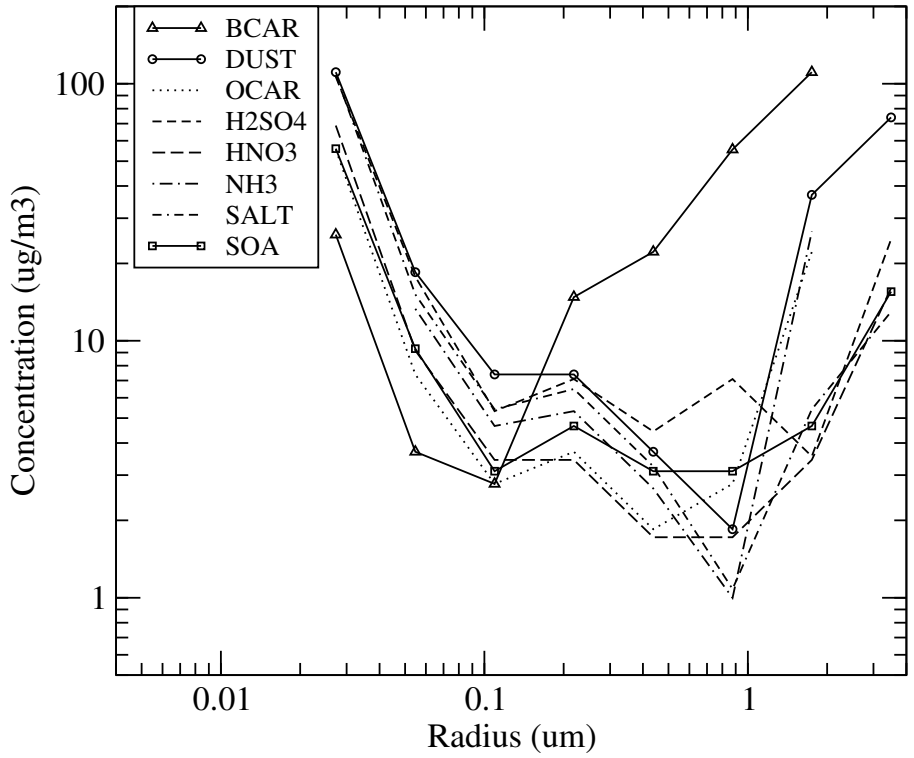

Fig. 6. Theoretical minimum detectable concentration ($\mu g\,m^{-3}$) per size section corresponding to $R' \geq 1.2$ (CALIOP night-time threshold) for each of the aerosol species considered by the model. Concentrations are considered at altitudes between ~ 700 and ~ 1200 m.

GMDD
5, 1691–1741, 2012

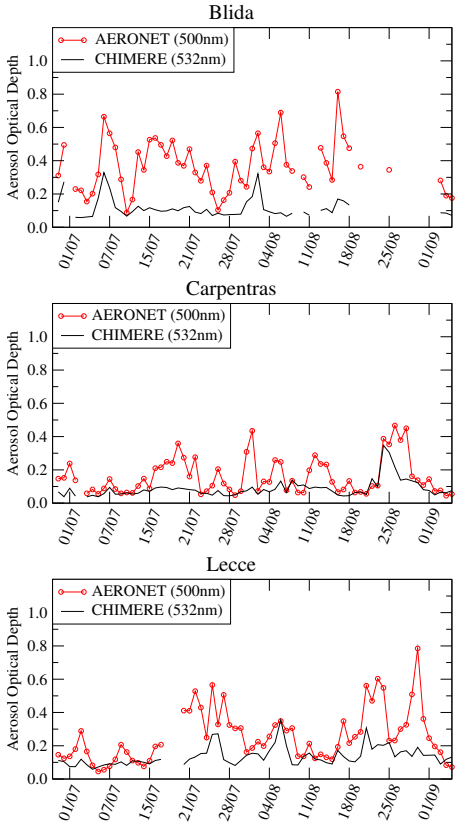

Fig. 7. Temporal evolution of the daily mean AOD (500 nm) by AERONET (red line) and the corresponding CHIMERE AOD (at 532 nm, black line) at three AERONET sites (Blida, Carpentras, Lecce).

GMDD
5, 1691–1741, 2012

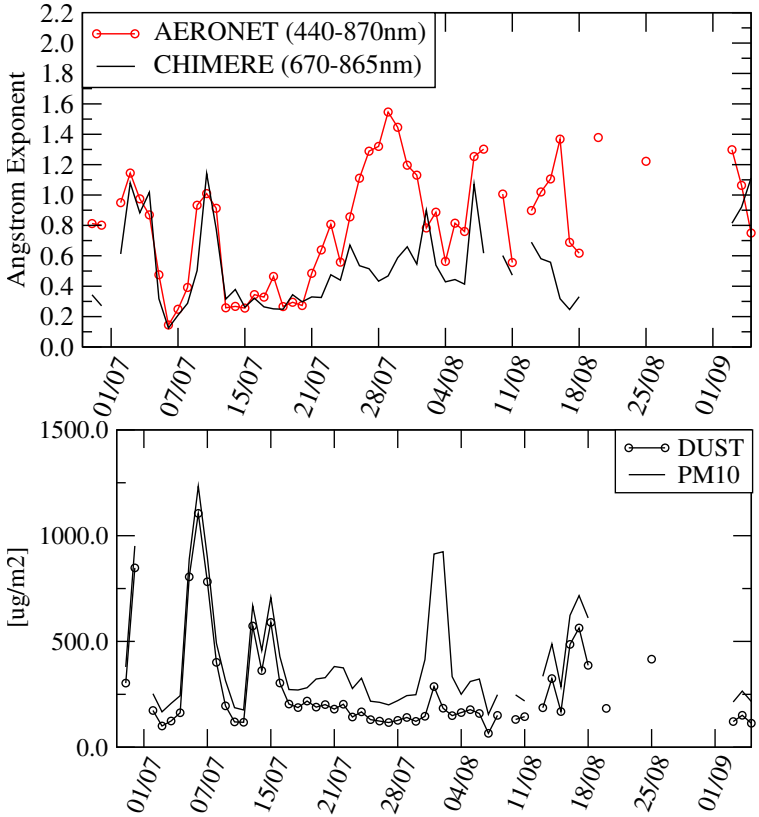

Fig. 8. Temporal evolution of the daily mean and Angström exponent (440–870 nm) for the AERONET station in Blida (2.88° E, 36.5° N) between 29 June and 6 September 2007 and the corresponding CHIMERE Angström exponent (at 670–865 nm, red line). The daily mean (for the same hours as the measurements) dust and PM_{10} concentrationis shown in the bottom figure.

GMDD
5, 1691–1741, 2012

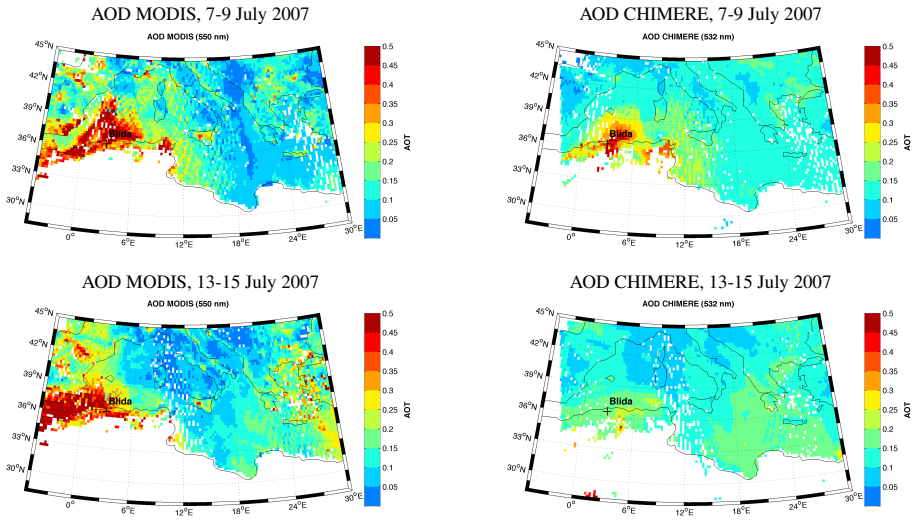

Fig. 9. Maps of mean AOD by MODIS (550 nm) and CHIMERE (532 nm) during the 7–9 and 13–15 July 2007 dust events. MODIS data are re-gridded to the resolution of the model.

GMDD
5, 1691–1741, 2012

Lidar signal simulation for the evaluation of aerosols

S. Stromatas et al.

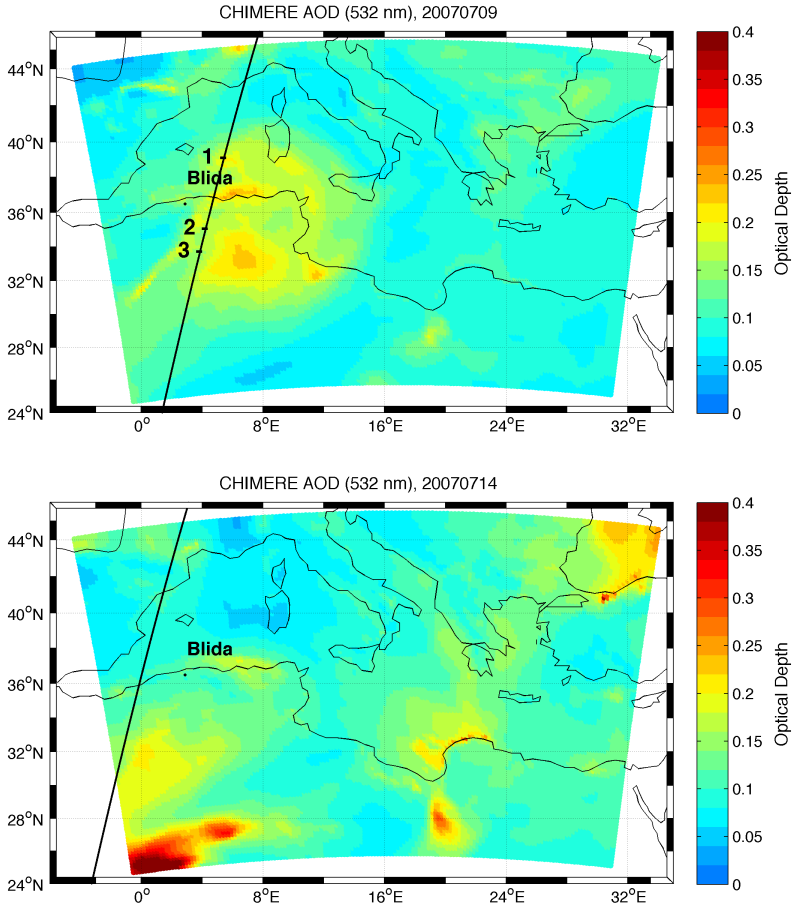

Fig. 10. Aerosol Optical Depth modeled with CHIMERE for $\lambda = 532\,\text{nm}$ for the 9 and 14 July 2007 at the same hour as the CALIPSO overpass time.

GMDD
5, 1691–1741, 2012

Lidar signal simulation for the evaluation of aerosols

S. Stromatas et al.

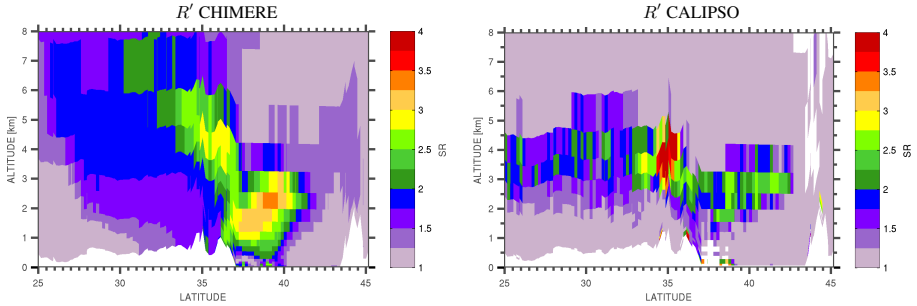

Fig. 11. Attenuated Scattering Ratio by CHIMERE **(a)** and CALIOP **(b)** for the nighttime portion of the orbit of the 9 July 2007. The initial profiles corresponding to cloud contaminated data are filtered out. The cloud-free data are averaged into the model's horizontal and vertical resolutions for comparison to the simulated $R'(z)$ profiles.

GMDD
5, 1691–1741, 2012

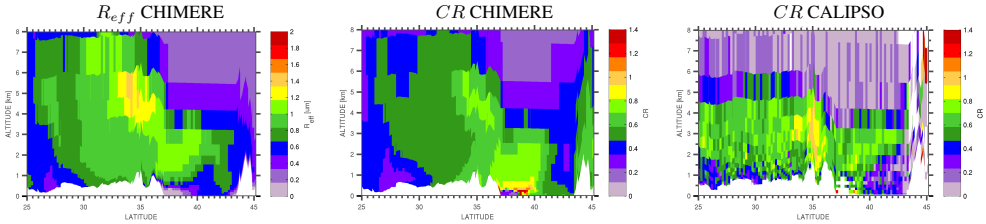

Fig. 12. Effective Radius and Color Ratio by CHIMERE **(a, b)** and Color Ratio CALIOP **(c)** for the nighttime portion of the orbit of the 9 July 2007. The initial profiles corresponding to cloud contaminated data are filtered out. The cloud-free data are averaged into the model's horizontal and vertical resolutions for comparison to the simulated $R'(z)$ profiles.

GMDD
5, 1691–1741, 2012

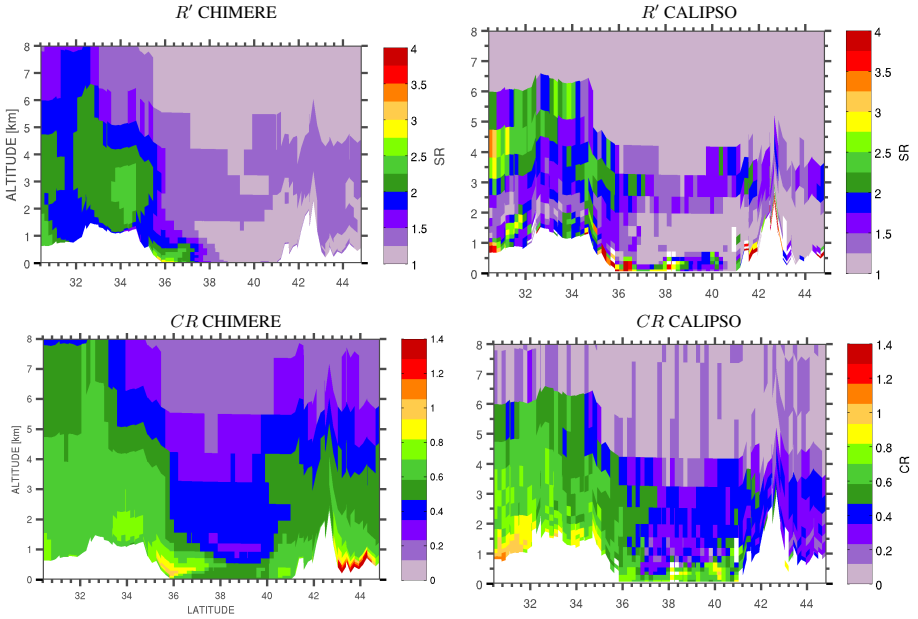

Fig. 13. Same as Fig. 11 but for the nighttime portion of the orbit of the 14 July 2007.

GMDD
5, 1691–1741, 2012

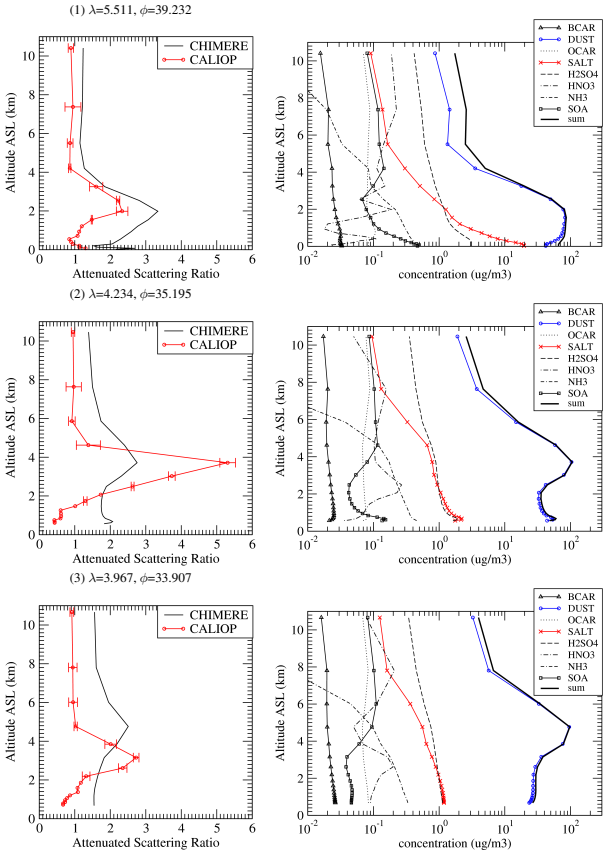

Fig. 14. Scattering Ratio profiles by CALIOP and CHIMERE (left) for the nighttime portion of the orbit the 9 July 2007 and the corresponding CHIMERE concentration profiles per species (right).

GMDD
5, 1691–1741, 2012